Process intensification in mass-transfer limited catalytic reactors through anisotropic periodic open cellular structures

Claudio Ferroni [a,b], Mauro Bracconi [a], Matteo Ambrosetti [a], Gianpiero Groppi [a], Matteo Maestri [a], Hannsjörg Freund [b,*], Enrico Tronconi [a]

[a] *Laboratory of Catalysis and Catalytic Processes, Dipartimento di Energia, Politecnico di Milano, via La Masa 34, Milano 20156, Italy*
[b] *Institute of Reaction Engineering and Catalysis, TU Dortmund University, Emil-Figge-Straße 66, Dortmund 44227, Germany*

ARTICLE INFO

ABSTRACT

We propose an advanced design of catalyst supports based on Periodic Open Cellular Structures (POCS) with a modified diamond unit cell. The diamond unit cell is modified by changing the angle between the struts and the fluid direction, thus changing the fluid-solid interaction and consequently the gas-solid mass and momentum transfer properties. Computational Fluid Dynamics is employed to fundamentally investigate the transport phenomena, and to carry out a parametric investigation of the effects of the morphological properties (i.e., struts angle, porosity and unit cell size). A drastic reduction of the friction factor (i.e., up to 50%) at moderate reduction of the mass transfer coefficient (i.e., up to 30%) is observed in the modified configuration upon progressively aligning the struts with the flow direction. This results in an overall improvement of the trade-off between the two properties leading to superior overall performances compared to state-of-the-art structured substrates. Unifying engineering correlations are then developed based on the numerical results for the evaluation of mass transfer coefficients and friction factors of the POCS, describing the behaviour of both the conventional and the modified cellular structure.

1. Introduction

Periodic Open Cellular Structures (POCS) or lattice materials were introduced as a new generation of catalyst substrates in the chemical reaction engineering community by Freund and co-workers about one decade ago [1]. Since then, POCS are receiving significant attention as innovative structured substrates for process intensification of catalytic reactors [2–12]. POCS are constituted by a regular ensemble of unit cells, with defined shape, filling the three-dimensional space in a periodic arrangement and permeable to fluid flow in all directions. In principle, the unit cell can assume any shape and is formed by an interconnected solid matrix of ligaments or struts that define open windows. The main advantage of such substrates is their reproducibility through additive manufacturing (AM), which allows for their high flexibility in design and fine tuning of the geometrical properties to tailor the POCS to the specific application. Advanced AM technologies enable to handle different materials that are required for substrates in catalytic applications, e.g., metals such as steel and aluminium or technical ceramics. Additionally, resin samples can also be

manufactured with the scope of non-reactive experiments [10,13] or reactive testing to evaluate fluid-solid transport properties [7]. Because of these features, POCS substrates have been envisioned for a variety of catalytic applications to overcome limitations associated with transport phenomena. In this perspective, metal-based POCS are suited for applications with demanding heat management thanks to their enhanced fluid-solid heat transfer [4,11,14,15] and effective conductivity [3,6,16] resulting in more compact, intensified reactors [5,6]. Conversely, ceramic-based POCS look attractive as a new generation of structured substrates for environmental applications (e.g., exhaust aftertreatment), where the reference supports employed are honeycomb monoliths [17–19]. Environmental applications are typically characterized by fast reactions that are severely limited by gas-solid mass transfer. Exhaust aftertreatment systems require a low pressure drop to minimize additional costs related to pollutants processing or to avoid engine penalties. Hence, POCS could successfully be applied as a replacement of the honeycomb monolith to ensure superior gas-solid mass transfer performance [14,17–19], and consequently higher abatement capacity. On the other hand, this was so far observed to come along with a corresponding

---

* Corresponding author.
E-mail address: hannsjoerg.freund@tu-dortmund.de (H. Freund).

increment of the pressure drop [13,17].

So far, few POCS designs (e.g., diamond, cubic, tetrahedral, Kelvin, octet-truss lattices) have been systematically investigated. The octet-truss lattice was investigated to enhance the convective heat transfer in compact heat exchangers [20–23]. Krishnan and co-workers experimentally [20] and numerically [21] investigated the convection mechanism and the fluid dynamic behaviour of the octet. The Kelvin unit cell has been extensively investigated, as often considered as an idealized unit cell for open cell foams [24–27]. Lucci et al. [24] studied convective mass transfer and pressure drop in Kelvin lattices and compared them with those of foams. They observed that the two cellular materials offered comparable geometrical properties, but higher fluid-solid mass transfer coefficients were obtained in the case of the Kelvin lattice at lower pressure drop than for the foam. Later, Sun et al. [25] confirmed and extended such results also in the case of convective heat transfer. Ferroni et al. [13,14] investigated the diamond and the Kelvin lattices fluid-solid transport properties. The trade-off between mass transfer and pressure drop was evaluated through the Merit Index, a dimensionless trade-off index proposed by Giani et al. [28], showing that the diamond lattice offers the best overall performance between the two. While such cell offered a better transport coefficient than the state-of-the-art structured honeycomb support [14], higher pressure drop was found as well. Overall, a worse trade-off than the honeycomb was found, hindering their adoption in environmental catalysis applications [13].

Nevertheless, the manipulation of POCS basic designs towards more advanced shapes represents an interesting option for the intensification of their performance. The approaches so far employed for advanced designs can be classified into the following categories: optimization of the lattice orientation with respect to the fluid flow [4,9,17]; generation of new cell shapes based on the combination of basic geometries [8,10, 12]; optimization of solid distribution within the unit cell [3]. Considering the first approach, Papetti et al. [17] showed that gas-solid transport properties of POCS are primarily function of the unit cell shape. By changing the lattice orientation with respect to the fluid flow direction, it is possible to increment the performance of a given unit cell. For instance, the tilted-cubic unit cell was proven to offer superior performance compared with the same shape aligned to the flow direction (i.e., 30% higher Merit Index). However, according to the results of Ferroni et al. [13,14], the diamond lattice offers an even better performance index than the tilted-cubic unit cell at same porosity equal to 0.9 (up to 0.4 vs. up to 0.3). Along the same lines, Dubil et al. [4] numerically investigated four configurations of the cubic unit cell (i.e., simple, staggered, inclined and double inclined). The double inclined configuration was proven to offer the highest gas-solid heat transfer coefficient, in full agreement with Papetti et al. [17]. With reference to the second approach, Freund and co-workers proposed advanced POCS solutions to improve flow distribution in multi-phase reactor environments [8,10, 12]. They proposed a hybrid unit cell by combining the Kelvin and the diamond shapes, the so-called DiaKel unit cell, for improving the liquid distribution inside multiphase systems [10,12]. Later on, they proposed the concept of interPOCS [8], i.e., two interpenetrating yet unconnected and freestanding POCS. This geometrical arrangement allows for changing the relative position of one structure in operando according to the desired flow behaviour inside the catalytic reactor. Finally, a last approach has been proposed, consisting of properly adjusting the solid distribution within the unit cell [3]. In doing so, a POCS having different window sizes, permeability and transport properties along different directions is obtained. For instance, a cubic unit cell was considered by Bracconi et al. [3] with different strut thickness in either the streamwise or transverse coordinates. As a result, the effective conductivity in the axial or radial direction can be tuned for improving processes with demanding heat management. Such a concept of anisotropic POCS can be transferred to the diamond lattice in view of the intensification of its performance in mass-transfer limited catalytic reactors.

In this work, we envision a different advanced POCS design strategy specifically for the intensification of catalytic reactors driven by a trade-off between the gas-solid heat and mass transfer and pressure drop, such as encountered in environmental applications [13]. The diamond lattice is modified by changing the angle between the struts and the fluid flow direction. Accordingly, the unit cell can be stretched or shrunken along the flow direction, modifying the fluid-solid interaction and consequently the transport properties and friction factor. In doing so, an anisotropic lattice is obtained, which enables to boost the diamond lattice overall performance evaluated in terms of Merit Index [13]. The fluid dynamic behaviour inside the modified diamond lattice is assessed numerically through reactive Computational Fluid Dynamics simulations.

2. Geometrical models

A modified diamond lattice is considered as an evolution of the regular geometry [8,10,13,14]. Fig. 1 depicts the regular and the modified lattice unit cells. To obtain the modified structure, the angle of attack of the struts is modified, i.e., the angle α between the struts of the unit cell and the fluid direction z (see Fig. 1), thus achieving a different fluid-solid interaction. Notably, for the regular lattice α^*_{Dia} is equal to $\arctan(\sqrt{2})$, 54.7°. Instead, for the modified lattice an α < 54.7° leads to a stretched unit cell along the z direction as illustrated in Figure 1(b), while an α > 54.7° leads to a shrunken one as shown in Figure 1(c). The modified lattice is obtained by translating the nodes along the axial direction z at constant strut length. In doing so, a rigid rotation of the struts is obtained around their nodes. Hence, the cubic-shaped unit cell which is circumscribed to the diamond unit cell (Figure 1(a)) having cell size d_c is deformed to a parallelepiped (Figure 1(b)-(c)).

As discussed in previous works [13,14], the regular diamond lattice is fully defined by two independent geometrical parameters, e.g., the porosity ε and the cell size d_c. Hence, for the modified diamond lattice, the porosity ε and the equivalent cell size d_c defined as the size of the regular diamond lattice featuring the same strut length (see Eq. (1)) are employed in consistency with [13,14], and the parameter α is additionally introduced.

$$d_c = \frac{4}{\sqrt{3}} l_s \tag{1}$$

The equivalent cell size is thus introduced to sketch out the effect of α on the unit cell deformation by rigid rotation of the struts around the nodes (see Fig. 1), also obtaining a translation of the nodes along the streamwise direction. The two unit cell sizes $d_{c,z}$ and $d_{c,xy}$ (see Figure 1 (b)-(c)) defining the unit cell size along the z and the x-y coordinates, respectively, are related with the strut length l_s and the equivalent cell size d_c by the following equations:

$$d_{c,xy} = 2\sqrt{2} \cdot \sin(\alpha) \cdot l_s = \sqrt{\frac{3}{2}} \sin(\alpha) \cdot d_c \tag{2}$$

$$d_{c,z} = 4 \cdot \cos(\alpha) \cdot l_s = \sqrt{3} \cos(\alpha) \cdot d_c \tag{3}$$

Detailed geometrical models are required for the systematic investigation of the transport properties of the modified diamond unit cell. In particular, models for the prediction of the strut diameter d_s and specific surface area S_v were developed and are reported in Table 1 (see Supporting Information, Section S1 for further details).

The strut diameter and the specific surface area are discussed as a function of the independent geometrical properties α and d_c. The d_s and S_v are respectively linearly and inversely proportional to the cell size. Therefore, the dimensionless quantities $d_s d_c^{-1}$ and $S_v d_c$ are examined as a function of the angle α in Fig. 2, while an analogous dependency on the porosity as reported in [14] for the regular diamond lattice is found for the modified lattice. Additionally, the volume shrinking factor of the unit cell V_{cell}/V_{Dia}, being V_{Dia} the volume of the regular lattice at the same equivalent cell size d_c, is analysed.

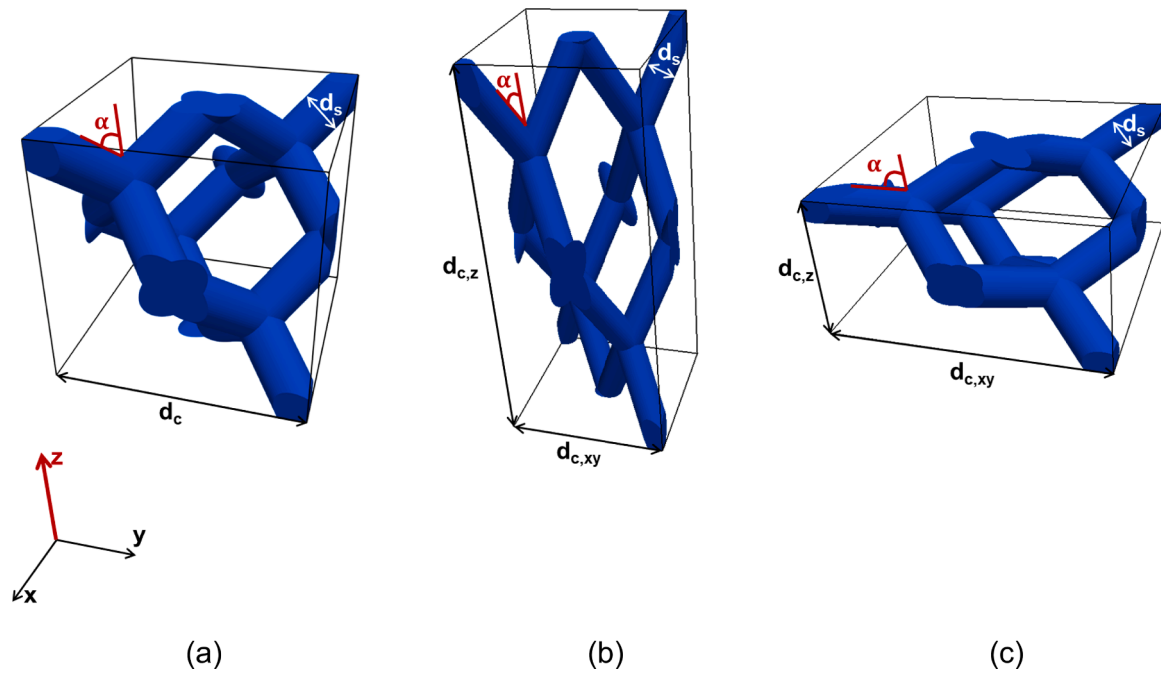Fig. 2(a) shows that, at constant cell size, the volume of the unit cell

Fig. 1. Modified diamond lattice configurations. (a) Regular diamond unit cell whose $\alpha = 54.7°$, modified unit cell (b) with $\alpha < 54.7°$ and (c) with $\alpha > 54.7°$ obtained by re-orienting the struts along the working fluid direction z (marked in red).

Table 1
Geometrical model for the modified diamond lattice.

Porosity	$\varepsilon = 1 - \dfrac{2}{3\sqrt{3}} \dfrac{\pi d_s^3}{d_c^3 \cos(\alpha)\sin^2(\alpha)} \left(\sqrt{3}\, \dfrac{d_c}{d_s} + \dfrac{0.871}{\tan(\alpha)} - \dfrac{1.733}{\sin(\alpha)} \right)$
Specific surface area	$S_v = \dfrac{\frac{8\pi}{3\sqrt{3}} d_s^2}{d_c^3 \cos(\alpha)\sin^2(\alpha)} \left(\sqrt{3}\, \dfrac{d_c}{d_s} + \dfrac{0.820}{\tan(\alpha)} - 1.277 \cdot \dfrac{\frac{\pi}{2} - \alpha}{\sin(\alpha)\cos(\alpha)} - 1.277 \right)$

V_{cell} (dashed line) is maximum for the regular diamond lattice (Figure 1 (a)). Consequently, at constant porosity, the strut diameter (solid black line) is maximum for the regular diamond lattice. Because of this reason, minimum surface area is offered by the regular geometry. It is worth

noticing that for $\alpha \to 0°$ and $\alpha \to 90°$ the unit cell degenerates to a planar geometry, therefore, a degenerated unit cell volume is obtained and $d_s \to 0$ and $S_v \to +\infty$. Remarkably, the discussed effects of Fig. 2 hold for prescribed d_c, ε. Conversely, if we considered constant d_s, almost a constant S_v would be obtained for all the structures at the different α. Indeed, by combining the equations of the model (see Table 1), the following relationship can be obtained:

$$S_v \approx 4 \cdot \frac{1 - \varepsilon}{d_s} \tag{4}$$

which is in agreement with our observations for the regular diamond cell [13]. In this case, the volume of the unit cell is minimum for $\alpha = \alpha^*_{Dia}$ according to the following relationship:
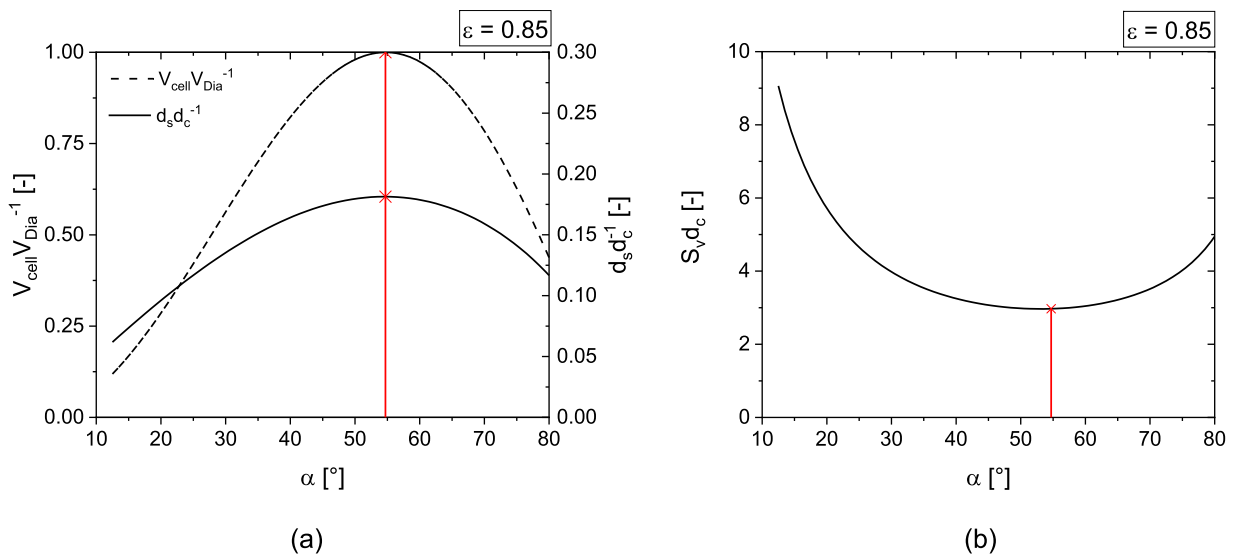

Fig. 2. (a) $d_s d_c^{-1}$ and $V_{cell} V_{dia}^{-1}$ (solid and dashed line, respectively) and (b) $S_v d_c$ against the modified diamond lattice angle α at constant cell size d_c and porosity $\varepsilon = 0.85$. Red line: regular diamond lattice.

$$V_{cell} = \frac{3\sqrt{3}}{2}d_c^3 \cos(\alpha)\sin^2(\alpha) = \frac{\pi d_s^3}{1-\varepsilon}\left(\sqrt{3}\ \frac{d_c}{d_s} + \frac{0.871}{\tan(\alpha)} - \frac{1.733}{\sin(\alpha)}\right) \tag{5}$$

In our previous work, a Hagen-Poiseuille-like equation was proposed for the prediction of pressure drop in POCS [13], which is also hereby adopted for the modified lattice configuration (see the following Section 3.2). The POCS virtual channel size is required for the modelling, corresponding to the size of the POCS windows projected along the streamwise direction $d_{w,T}$. In the case of the regular diamond unit cell, the $d_{w,T}$ was geometrically determined equal to $d_c/2$-d_s. In this work, to account for the effect of the α on the restriction of the unit cell cross-sectional area, the $d_{w,T}$ is obtained after geometrical analysis reported in Supporting Information, Section S2 and equals to:

$$d_{w,T} = \sqrt{2}l_s \cdot \sin(\alpha) - d_s = \frac{\sqrt{6}}{4}d_c \cdot \sin(\alpha) - d_s \tag{6}$$

Note that when $\alpha = \alpha^*_{Dia}$, the same expression as reported in [13] is obtained for the regular diamond unit cell. Such a definition of the $d_{w,T}$ was confirmed by analysis of the streamlines of the flow crossing the unit cell windows, as reported in Supporting Information, Section S2.

The geometrical properties of the samples employed for fundamental investigation are reported in Supporting Information, Section S3.

3. Numerical methods

3.1. CFD modelling

The fundamental investigation of gas-solid mass transfer and pressure drop in the modified diamond lattice is carried out through detailed CFD simulations using the catalyticFOAM framework [29,30]. In particular, reactive CFD simulations are coupled with the DAKOTA numerical toolkit from Sandia [31], to exploit them as in-silico experiments. Steady-state simulations are carried out to solve the Navier-Stokes equations and the species mass balances. Since isothermal conditions are always considered, the energy balance can be neglected. The methodology was already employed and experimentally validated for the investigation of open-cell foams [32,33] and POCS [13,14] and is hereby briefly reported (full details in [13,14,32,33]). At the POCS catalytic surface, the net production or consumption rates are assumed to be equal to the local mass fluxes due to the species diffusion [29]. CO oxidation in air is employed as a case study with CO as mass transfer limited reactant and with a first order reaction in CO. An infinitely fast heterogeneously catalysed reaction is assumed at the catalytic wall. To do so, the kinetic constant is set to achieve a Damköhler number > 1000, resulting in gas-solid mass transfer limitation of the test reactant CO. A feed mixture of CO = 3 vol.-% in air at T = 293.15 K and an outlet pressure of p = 1 bar is considered.

A second-order upwind scheme (linear upwind) and a pure second-order scheme are employed for the discretization of the convective and diffusive terms, respectively. The thermodynamic and transport properties adopted for the analysis of the CFD data are evaluated through the catalyticSMOKE [30] and OpenSMOKE++ [34] libraries. The thermodynamic properties of the gas species are estimated using the approach by Gordon and McBride [35] and are exploited to compute the gas mixture properties using the Gibbs theorem. The transport properties are evaluated by means of standard kinetic theory expressions [36,37].

POCS numerical domains are obtained by means of the snappy-HexMesh in-built utility of the OpenFOAM framework [38]. Details on the meshing and mesh convergence analysis are reported in [13,14]. In this work, a mesh convergence analysis was carried out aiming at verifying the adequacy of the mesh resolution for the fundamental investigation of the modified diamond lattice behaviour, and the results are reported in Supporting Information, Section S4. The modified diamond lattice is investigated in fully developed flow and concentration regimes. To do so, periodic boundary conditions are implemented for all relevant variables following the approach reported in [14], thus allowing to neglect side effects as entrance and solid wall confinement effects. On top of this, periodic boundary conditions allow to employ computational domains consisting of only a few POCS unit cells [14]. In particular, the POCS unit cell was identified as Representative Elementary Volume (REV) of the lattice geometrical features and fluid dynamic behaviour [13,14]. In this work, an REV analysis was carried out confirming this outcome also in the case of the modified diamond lattice, and the results are reported in Supporting Information, Section S4. Asymptotic conditions are deemed to be representative of the catalytic reactor behaviour, whose size is generally orders of magnitude larger than the size of the POCS unit cell.

Steady-state simulations and transient simulations are employed respectively for the prediction of the POCS fluid dynamic behaviour in laminar and unsteady laminar regime, the former requiring around 200–300 cpu hours and the latter around 3000–5000 cpu hours on 96 processors. In this work, a total of 280 simulation runs were carried out.

3.2. Analysis of the transport coefficients

A conventional 1D, heterogeneous, isothermal, plug flow reactor model in steady-state conditions is employed for the interpretation of the gas-solid mass transfer simulation results [14,33,39–41]. Because gas-solid mass transfer limited conditions are imposed, the CO mass fraction at the solid surface is set to zero and only the fluid phase mass balance is considered for CO:

$$-u \cdot \rho \cdot \frac{d\omega_{CO}}{dz} = k_{MAT} \cdot S_v \cdot \rho \cdot \omega_{CO} \tag{7}$$

where u is the working fluid velocity, ρ is the fluid density, ω_{CO} is the CO mass fraction, z is the streamwise coordinate and k_{MAT} is the gas-solid transport coefficient.

Following the hypotheses reported in [14,33] and introducing the POCS strut diameter as characteristic length d_s in consistency with [13, 14,32,33], it is thus possible to evaluate the Sherwood number, Sh_{d_s}:

$$Sh_{d_s} = \frac{k_{MAT} \cdot d_s}{\mathfrak{D}_{CO}} = -\frac{\ln(1-X_{CO})}{S_v \cdot L} \cdot \frac{ud_s}{\mathfrak{D}_{CO}} \tag{8}$$

where X_{CO} is the CO conversion, L is the domain length and $\mathfrak{D}_{CO}$ is the CO diffusivity in air. The cup-mix average mass fractions of CO at the inlet and outlet of the domain from CFD simulations are employed to compute X_{CO} [14,33,42].

CFD simulations allow also for the evaluation of the friction factor. In agreement with [13], it is defined as:

$$\phi_{d_s} = \frac{\Delta p}{L} \cdot \frac{d_s}{\rho u^2} \tag{9}$$

where Φ_{ds} is the friction factor with d_s as characteristic length and Δp is the pressure drop evaluated in CFD.

It is worth noticing that both the friction factor and the dimensionless mass transfer coefficient are a function of the substrate geometry and *Re*. The Merit Index (M.I.) by Giani et al. [28] is calculated to evaluate the overall performances of substrates in terms of trade-off between conversion and pressure drop under mass transfer controlled conditions. The M.I. is a dimensionless trade-off index which weighs the mass transport coefficient to the friction factor in the following form:

$$M.I. = -\frac{\ln(1-X_{CO})}{\frac{\Delta p}{\rho u^2}} = \frac{L_{char} \cdot S_v \cdot Sh_{Lchar}}{\phi_{L_{char}} \cdot Re_{L_{char}} \cdot Sc} \tag{10}$$

where L_{char} is the characteristic length (d_s in the case of POCS), *Sc* is the Schmidt number and *Re* is the Reynolds number.

4. Results

4.1. Appraisal of the modified diamond lattice overall performance

The modified diamond lattice is initially checked to verify the effect of geometrical manipulation on the trade-off between gas-solid mass transfer properties and pressure drop, aiming at defining an operation window of α where an increment of the performance is found. As demonstrated in [13,32], the M.I. is function of the POCS porosity and the Reynolds number. A monotonic increase of the M.I. was found at increasing porosity at constant Re [13], while a maximum M.I. is achieved at around $Re \cong 10$. In the case of the modified diamond lattice, the struts tilting angle α is additionally introduced as free parameter (see Section 2). Hence, for the preliminary evaluation of the M.I., a fixed porosity $\varepsilon = 0.9$ is chosen, while the effects of Re_{ds} and α are examined in detail as illustrated in Fig. 3.

Fig. 3 shows that the M.I. increases by decreasing α, namely, for a stretched lattice (see Fig. 1(b)) along the streamwise direction. The state-of-the-art structured support, i.e., the honeycomb monolith, offers a M.I. equal to 0.4 at the porosity/OFA of 0.85 [13,32]. In this perspective, a wide operative window of α and Re_{ds} exists where a higher M.I. than for the honeycomb is obtained, i.e., for α<45°. Moreover, a twice as high M.I. compared to the regular diamond lattice and the honeycomb is obtained at α<20°. Notably, at decreasing α, the maximum M.I. is obtained at higher Re_{ds} than for the regular geometry. For instance, a maximum M.I. = 0.8 is obtained at $\alpha \cong 20°$, $Re_{ds} \cong 20$ against the maximum value of M.I. = 0.4 attainable for the regular diamond lattice at $Re_{ds} \cong 10$.

The modified diamond lattice thus offers high potential for increasing the trade-off index with a factor of up to 2 for $\alpha < \alpha^*_{Dia}$. Hence, in the following Sections the modified lattice is further investigated for $\alpha < \alpha^*_{Dia}$ aiming at understanding the effect of such parameter on the mass transport properties and on the friction factor.

4.2. Effect of the struts tilting angle

In this Section, the Sherwood number and the friction factor are examined as a function of the struts' angle of attack α. Moreover, the effect of α on the flow regimes is analysed. To do so, samples of porosity between 0.7 and 0.95, cell size between 1 mm and 8 mm and angle 12.5° $< \alpha < \alpha^*_{Dia}$ were generated (Supporting Information, Table S1). The effect of the angle α is examined for porosity $\varepsilon = 0.9$ and $d_c = 1$ mm for 4

$\leq Re_{ds} \leq 200$.

Fig. 4(a) shows the Sherwood number Sh_{ds} against the Reynolds number Re_{ds} at variable α. The Sh_{ds} increases with Re_{ds} for all the considered geometries. In the case of the regular diamond lattice, a dependency of Sh on $Re^{0.33}$ is obtained between $4 \leq Re_{ds} \leq 32$ (see Fig. 4 (a)), which is typical of flow around submerged objects in the laminar regime [33,43–45]. At increasing Re_{ds}, a steeper increase of Sh_{ds} is observed, with a dependency of Sh_{ds} to $Re^{0.45}$ due to the onset of vortex shedding for $Re_{ds} > 32$ [14]. Differently, in the case of α = 20°, a dependency of Sh on $Re^{0.33}$ is observed up to $Re_{ds} \leq 64$, while an increment of the exponent to $Re_{ds}^{0.39}$ is observed at higher Re_{ds}, which is, however, still a lower value than the one of the regular cell.

Fig. 4(b) shows that Sh_{ds} increases with α at constant Reynolds number. This is ascribed to the fact that the struts are more aligned with the fluid flow at low α, thus resulting in a lower fluid-solid interaction. Longer and thinner struts are obtained by decreasing α (see Fig. 2(a)), therefore, a greater contribution of the strut and a lower contribution of the node to the overall surface area are obtained. On top of this, the effect of α is more pronounced at increasing Re. At $Re_{ds} = 8$, a dependency of Sh_{ds} on $\alpha^{0.3}$ is obtained. Then, an increased dependency on α is obtained at progressively increasing Re_{ds}, up to a dependency of Sh_{ds} on $\alpha^{0.55}$ at $Re_{ds} = 200$. Consequently, an interdependency of Sh_{ds} to α and Re_{ds} is obtained. This is ascribed to the fact that by decreasing α the transitional Re_{ds} between the laminar and unsteady laminar regimes (i.e. onset of vortex shedding) increases. Fig. 5(a) shows the streamlines of the flow at $Re_{ds} = 64$ for the regular diamond lattice. As reported in previous works [13,14], the regular diamond lattice was found to show a laminar regime for $Re_{ds} \leq 32$, while an unsteady laminar regime was found at higher Re_{ds}. Conversely, the modified diamond lattice with α = 20° shows a laminar regime even at such Re_{ds} as reported in Fig. 5(b). Such behaviour is ascribed to the tilting of the strut with respect to the fluid direction. Indeed, at lower α the struts are more aligned to the flow direction and, consequently, they offer less resistance to the fluid flow. In this view, reducing α results in a laminarization of the flow in the lattice even at higher Re than in the regular lattice. Hence, the transition between the regimes occurs at higher Re_{ds} and a lower fluid-solid interaction is thus achieved. This is reflected in the Sh_{ds} (see Fig. 4), as by decreasing α the dependency of Sh_{ds} on $Re_{ds}^{0.33}$ is preserved at higher Re_{ds} (i.e., $Re_{ds} < 32$ in the case of $\alpha = \alpha^*_{Dia}$ and $Re_{ds} < 64$ in the case of α=20°), and a steeper slope is observed at higher Re_{ds} in the case of the regular lattice.

Fig. 6 shows the friction factor Φ_{ds} against Re_{ds} of the same structures. The Φ_{ds} decreases with Re_{ds} for all the structures as typically achieved by submerged objects in cross flow [20,44–48]. In particular, a dependency of Re_{ds}^{-1} can be observed at $Re_{ds} < 32$ while dependencies of $Re_{ds}^{-0.4}$ for the regular diamond and $Re_{ds}^{-0.7}$ for α = 20° are obtained at higher Re. In analogy with Sh_{ds}, Φ_{ds} decreases with α, and an interdependency between Re_{ds} and α can be observed. For the regular diamond lattice, the dependency of Φ_{ds} on Re_{ds}^{-1} is obtained for $Re_{ds} \leq 32$ in the laminar regime. For the modified diamond lattice with α = 20°, the dependency of Φ_{ds} on Re_{ds}^{-1} is conserved up to $Re_{ds} \leq 64$, where the transition between the laminar and the unsteady laminar regime is achieved. Notably, the Φ_{ds} of the modified lattice decreases with α both in the laminar regime ($Re_{ds} \leq 64$) and in the unsteady laminar regime. In the first regime, this is ascribed to the longer and thinner struts obtained at low α (see Fig. 2(a)), which results in a larger contribution of the strut to the overall surface area and a lower contribution of the node. Thus, the skin friction is mainly determined by the strut and a lower contribution of the node skin friction is obtained. In the unsteady laminar regime, the aligned struts of the modified diamond lattice offer less drag to the fluid flow. In this view, both the viscous and inertial contributions to the pressure drop decrease at decreasing α.

In conclusion, the decrease of α results in a decrease of the fluid-solid interaction inside the modified diamond lattice which is reflected both in Sh_{ds} (Fig. 4) and Φ_{ds} (Fig. 6). This is obtained both in the laminar regime ($Re_{ds} \leq 64$) and in the unsteady laminar regime. Overall, this
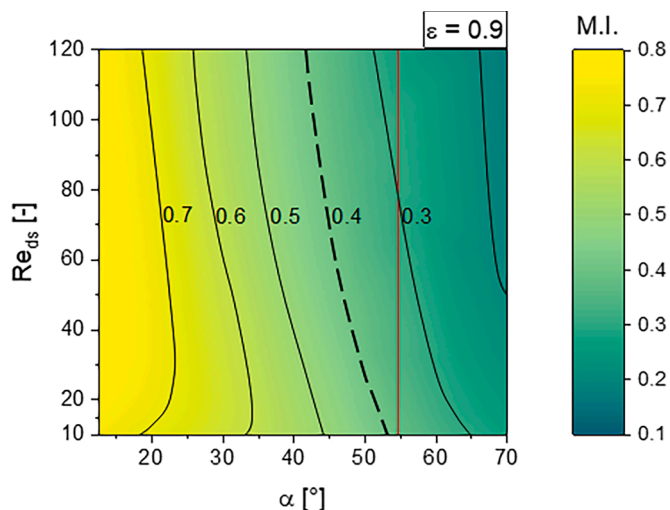

Fig. 3. Contour plot of the Merit Index of the modified diamond lattice as a function of the angle α and the Reynolds number Re_{ds} at porosity $\varepsilon = 0.9$. Black lines: level curves, red line: regular diamond lattice, dashed line: reference honeycomb M.I.
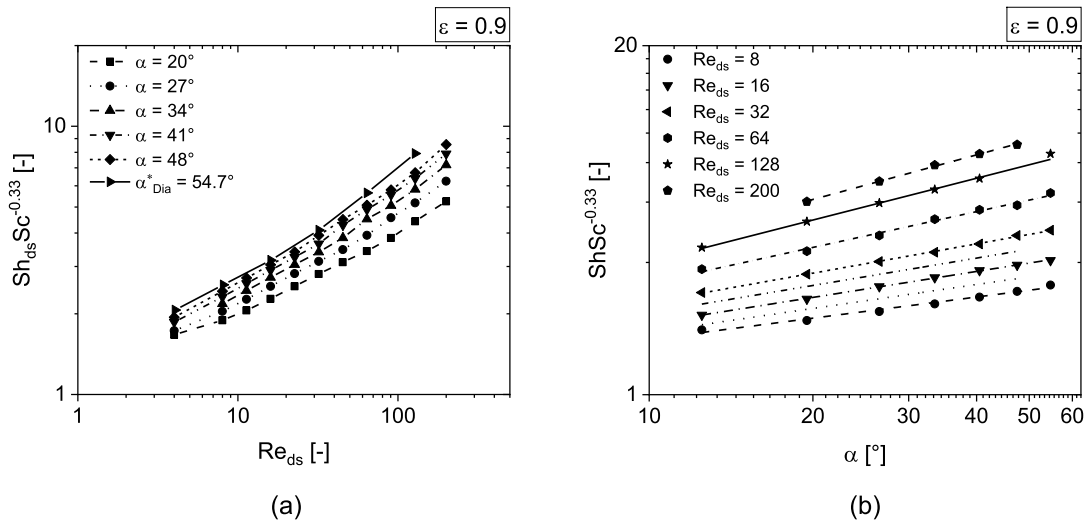
Fig. 4. Sherwood number of the modified diamond lattice (a) against the Reynolds number at changing α and (b) against α at changing Re_{ds} for porosity ε = 0.9.
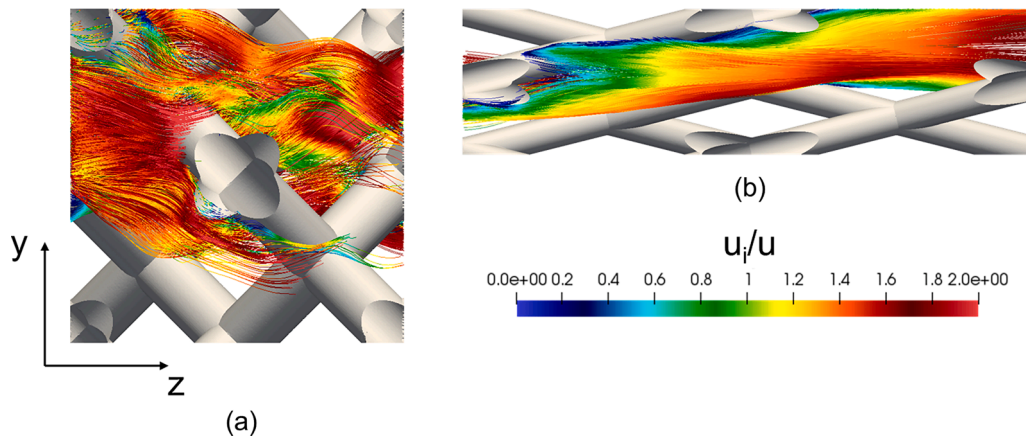

Fig. 5. Streamlines of the flow at Re_{ds}=64 (a) of the regular diamond lattice and (b) of the modified diamond lattice α = 20° (z, y streamwise and transverse coordinates, u_i/u interstitial velocity over the superficial velocity).
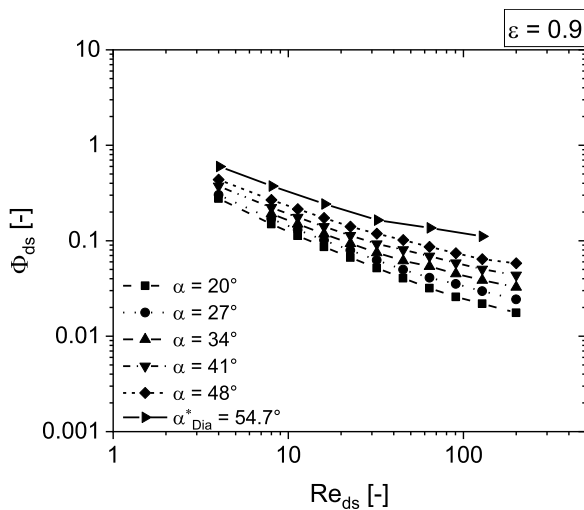

Fig. 6. Friction factor of the modified diamond lattice as a function of the Reynolds number and the struts tilting angle α for porosity ε = 0.9.

benefits the trade-off between them as proved in the preliminary analysis of Section 4.1.

4.3. Effect of the cell size and porosity

The Sherwood number and the friction factor are examined as a function of the porosity and cell size. To do so, the same samples of Section 4.2 (i.e., 1 mm ≤ d_c ≤ 8 mm, 0.7 ≤ ε ≤ 0.95, 12.5° ≤ α ≤ $α*_{Dia}$) are considered (Supporting Information, Table S1).

Fig. 7 shows (a) the Sherwood number and (b) the friction factor plotted against the Reynolds number for the angle α = 20° and porosity ε = 0.9, analogous behaviour is observed for the other geometries. Fig. 7 shows that the Sherwood numbers and friction factors are independent of the cell size as they overlap at each *Re*. In this view, the characteristic length, i.e., the strut diameter d_s, is linearly dependant on the cell size at constant porosity and angle (see Table 1). Hence, Sh_{ds} and $Φ_{ds}$ are dimensionless quantities whose dependency on the cell size is indirectly accounted for by their dependency on Re_{ds}. This was already observed for the regular diamond lattice as well [13,14].

In our previous work, an empirical dependency of Sh_{ds} on $ε^{-1.5}$ was found for the regular diamond lattice [14]. Fig. 8(a) shows $Sh_{ds}ε^{1.5}$ against the Reynolds number for the modified lattice with α = 20° (black) and α = 34° (red) at changing porosity 0.7 < ε < 0.9. The dependency of Sh_{ds} on $ε^{-1.5}$ well reconciles the Sh_{ds} data at different
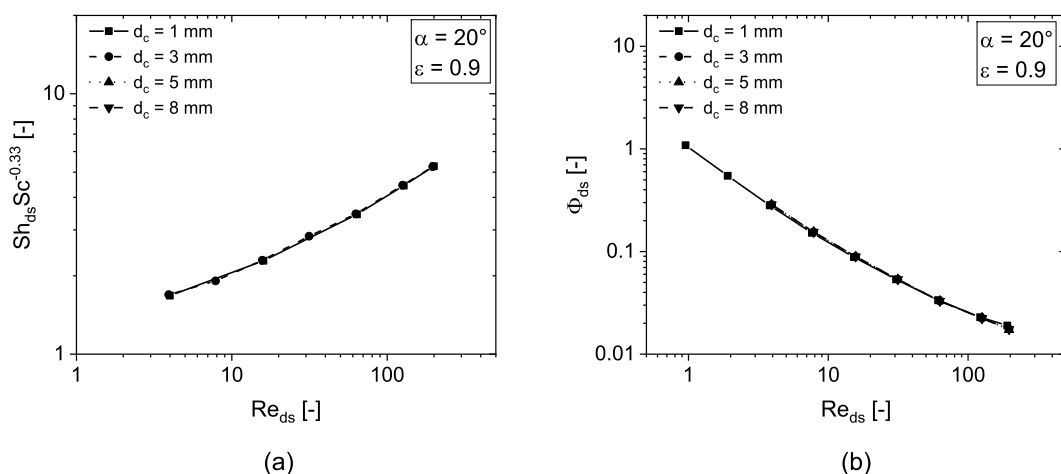
Fig. 7. (a) Sherwood number and (b) friction factor of the modified diamond lattice against the Reynolds number at changing cell size $1 \leq d_c \leq 8$ mm ($\alpha = 20°$, $\varepsilon = 0.9$).
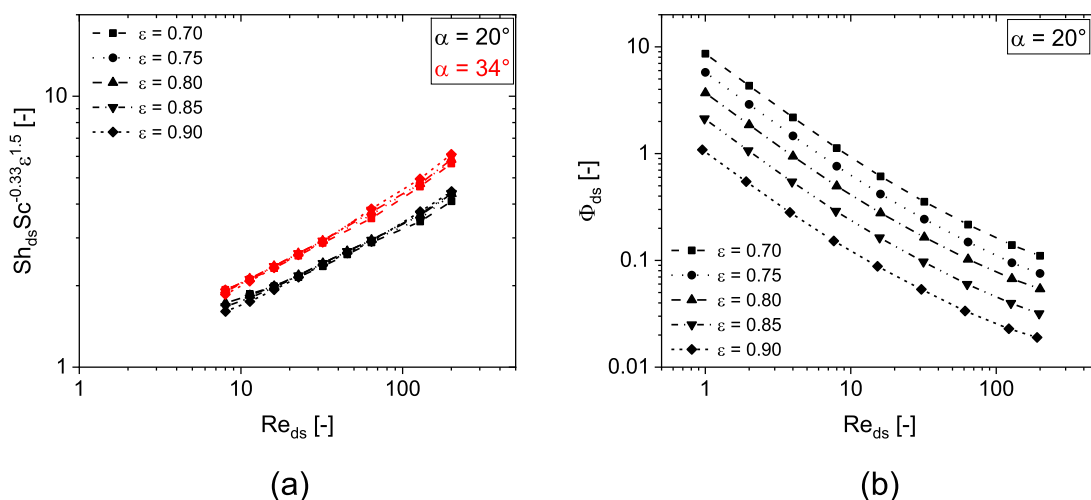

Fig. 8. (a) Sherwood number and (b) friction factor of the modified diamond lattice against the Reynolds number at changing porosity $0.7 \leq \varepsilon \leq 0.9$.

porosity at each considered angle, in fact, CFD data points overlap within $\pm$ 3% at each Re_{ds} and α. Therefore, Sh_{ds} decreases with the porosity increase in agreement with regular POCS [14] and with same functional dependency. Fig. 8(b) shows the friction factor against Re_{ds} for the modified lattice with $\alpha = 20°$. In analogy to regular POCS [13], Φ_{ds} decreases at increasing ε, both in the laminar and unsteady laminar regimes. At low Re_{ds}, this is ascribed to the lower specific surface area, resulting in lower skin friction. At high Re_{ds}, this is due to the thinner d_s which offer less drag.

5. Discussion

5.1. Mass transfer correlation

Section 4 revealed that the convection mechanism in the modified diamond lattice depends on the flow conditions, the POCS porosity and the struts' tilting angle with respect to the fluid flow. Conversely, the cell size is implicitly included by the functional dependency of the Sherwood number on the Reynolds number considering the strut diameter as the characteristic length. In particular, in the case of the porosity, an explicit dependency of Sh_{ds} on $\varepsilon^{-1.5}$ is on average found, in agreement with [14]. Instead, an interdependency on Re_{ds} and α was observed. A dependency of Sh_{ds} on $Sc^{1/3}$ is assumed following the boundary layer theory [36]. The present fundamental investigation was carried out for Sc around 1.

In the operating conditions of interest, the diamond unit cell POCS was found to offer two different flow regimes, namely a laminar regime and an unsteady laminar regime (see Section 4), and the transitional Re_{ds} between the two strictly depends on the geometry (i.e., on α). In addition to these two regimes, two additional ones are generally identified, namely the asymptotic conditions of creeping viscous flow and turbulent flow [49]. In this work, the effect of the flow conditions on the dimensionless mass transfer coefficient of the modified diamond lattice is thus modelled considering the two asymptotic contributions (i.e., related to creeping flow and turbulent flow) as proposed by Reichelt for fibrous materials [50] and in consistency with our previous work for the regular lattice [14] and for open-cell foams [33]. In particular, the laminar regime is modelled by using a functional dependency of Sh_{ds} on $Re_{ds}^{1/3}$, which is related to the creeping flow around submerged objects in cross-flow and well captures the modified diamond lattice behaviour as reported in Section 4.1, while the turbulent regime is modelled by using a dependency of Sh_{ds} on $Re_{ds}^{0.8}$, which is proposed for submerged objects in fully turbulent flow conditions [45,46]. In this view, the superposition of the two asymptotes led to an empirical dependency of Sh_{ds} on Re_{ds} raised to a power of 0.40–0.45 depending on α in the unsteady laminar regime (see Section 4.1), similar to a cylinder in cross flow [45] (i.e., $Re^{0.39}$ for $4 < Re \leq 40$ and $Re^{0.47}$ for $40 < Re \leq 4000$). Sh_{ds} exhibited an interdependency between Re_{ds}-α (see Section 4.1). This was ascribed to the fact that the fluid dynamics inside the modified diamond lattice

drastically changes at changing α. In particular, the transitional Re_{ds} between the laminar and unsteady laminar regime was observed to increase at decreasing α. Accordingly, the dependency of Sh_{ds} on $Re_{ds}^{1/3}$ is obtained at $Re_{ds} < 32$ for the regular diamond lattice and at $Re_{ds} < 64$ for the modified configuration with low α. Therefore, the two asymptotic contributions proportional to $Re_{ds}^{1/3}$ and to $Re_{ds}^{0.8}$ provide a different relative weight to the overall Sh_{ds} at changing α as a result of the change of the unit cell shape. Therefore, the combination of the asymptotic behaviour has to be properly weighted as a function of α. Hence, the following functional form is introduced:

$$Sh_{ds}Sc^{-1/3} = \varepsilon^{-1.5} \cdot \left(A(\alpha) \cdot Re_{ds}^{1/3} + B(\alpha) \cdot Re_{ds}^{0.8} \right) \tag{11}$$

A and B are evaluated at each α angle from regression of CFD data. The results are reported in Fig. 9. Notably, both A and B increase with α in agreement with the fundamental investigation (see Section 4.1). However, a steeper dependency of B on α than A can be observed, consistent with the evidence that the transition between the flow regimes is obtained at higher Re_{ds} on decreasing α.

An empirical dependency of $A(\alpha)$ and $B(\alpha)$ to α is proposed to account for the effect of the shape on the two asymptotic terms. In doing so, they are imposed to be equal to those of the regular diamond lattice for $\alpha = \alpha^*_{Dia}$, and a power law dependency is introduced to account for the effect of α:

$$A(\alpha) = 1.029 \cdot \left(\frac{\alpha}{\alpha^*_{Dia}} \right)^{m} \tag{12}$$

$$B(\alpha) = 0.022 \cdot \left(\frac{\alpha}{\alpha^*_{Dia}} \right)^{n} \tag{13}$$

Fig. 9 shows the regression of $A(\alpha)$ and $B(\alpha)$ as a function of α to evaluate m, n. The following engineering correlation is obtained:

$$Sh_{ds}Sc^{-1/3} = \varepsilon^{-1.5} \cdot \left(1.029 \left(\frac{\alpha}{\alpha^*_{Dia}} \right)^{0.3} \cdot Re_{ds}^{1/3} + 0.022 \left(\frac{\alpha}{\alpha^*_{Dia}} \right)^{1.9} \cdot Re_{ds}^{0.8} \right) \tag{14}$$

which holds for $1 \leq Re_{ds} \leq 200$, $0.7 \leq \varepsilon \leq 0.95$, $12.5 \leq \alpha \leq 54.7°$ and Sc around 1. Fig. 10(a) shows a parity plot comparing the model predictions and the CFD numerical data employed for the regression. A good agreement is obtained with a Mean Absolute Percentage Error (MAPE) equal to 3.9%. Based on previous results on open-cell foams and POCS [14,33], the developed mass transfer correlation can be extended to the estimation of gas-solid heat transfer coefficients following the Chilton-Colburn analogy for Pr around 1.

Eq. (14) well describes the interdependency of Re_{ds} and α as observed in Section 4.1. In particular, an empirical dependency of Sh_{ds} to $\alpha^{0.3}$ was
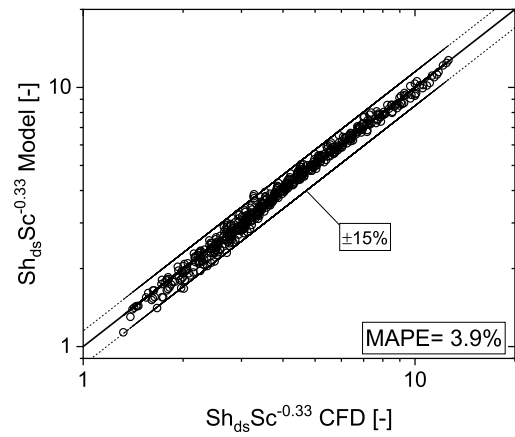

Fig. 10. Parity plot comparing the Sherwood number obtained from CFD simulations and the model prediction for the modified diamond lattice.

found in creeping flow (see Fig. 4(b)). Such a dependency progressively increases with Re_{ds} up to a dependency of Sh_{ds} to $\alpha^{0.55}$ at $Re_{ds} = 200$. This dependency results from the superposition of the two asymptotic contributions $(\alpha/\alpha^*_{Dia})^{0.3}$ and $(\alpha/\alpha^*_{Dia})^{1.9}$ of Eq. (14).

5.2. Pressure drop correlation

The present work revealed that the modified diamond lattice friction factor is a function of α, ε and flow conditions (see Section 4). In analogy with the mass transfer coefficient, the dependency of the friction factor on the unit cell size is implicitly accounted for by its dependency on the Reynolds number. Therefore, by considering the definition of the friction factor Eq. (9), the pressure drop can be described as:

$$\frac{\Delta p}{L} = \phi_{ds} \cdot \frac{\rho u^2}{d_s} = g(\varepsilon, \alpha, d_c, \mu, u) \tag{15}$$

where g is a generic function. To account for the effects of the fluid properties, a Darcy-Forchheimer expression is considered, which is generally employed for porous materials [51] and has been proposed by our group in the context of open-cell foams [32] and POCS [13]:

$$\frac{\Delta p}{L} = \frac{\mu u}{K} + \frac{\rho u^2}{\Gamma} \tag{16}$$

where K and Γ are the Darcian and non-Darcian permeabilities, respectively, and are only a function of the geometrical features of the
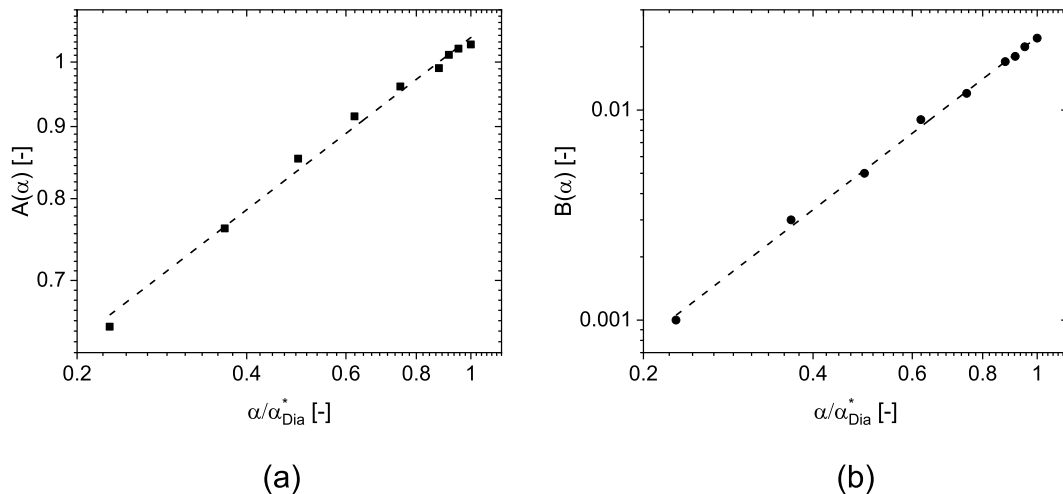

(a)

(b)

Fig. 9. Regression of the (a) A coefficient and (b) B coefficient of the Sh_{ds} as a function of α.

porous material. In this view, to account for the effects of the geometry on the pressure drop a modified Hagen-Poiseuille equation is proposed in agreement with [13]:

$$\frac{\Delta p}{L} = C' \cdot \frac{\mu u}{\varepsilon d_{w,T}^2} + D' \cdot \frac{\rho u^2}{\varepsilon^2 d_{w,T}} \qquad (17)$$

where $d_{w,T}$ is the tube diameter equivalent to the POCS window size available for the fluid flow, namely, the available opening on the streamwise direction (see Section 2), and C', D' are permeability constants.

In the Poiseuille equation, the permeability constants C and D are theoretical constants equal to 32 and 0.5 for ducts. In the case of the regular diamond lattice, the permeability coefficients C' and D' of the modified Poiseuille Eq. (17) were estimated as 9.89 and 0.25 [13] by regression of numerical and experimental data. Such values are lower than those of conventional tubes. This is ascribed to the fact that the POCS do not offer a continuous solid surface, but rather they are interpreted as an ensemble of parallel ducts offering a discontinuous solid surface which thus provides lower friction. In this work, the fluid dynamic behaviour of the modified diamond lattice was observed to drastically change by changing α (see Section 4.1). In particular, the transition between the laminar and unsteady laminar regime was obtained at higher Re_{ds} for decreasing α, with a simultaneous reduction of both the viscous and inertial term. Consequently, C' and D' of the modified data are evaluated from regression of CFD data at each angle in analogy to the transport coefficient (see Section 5.1). The result is reported in Fig. 11. Notably, even lower values of C' and D' are obtained at decreasing α in consistency with the observations of Section 4.1. Indeed, both the viscous and inertial terms of the friction factor are observed to decrease with α (see Fig. 6).

In analogy to the mass transfer analysis (see Section 5.1), an empirical dependency of C' and D' to α is proposed to account for such dependency of the two constants. To do so, the following aspect is considered. After the rigid deformation of the regular diamond to the modified diamond unit cell, the unit cell shrinks in the transverse coordinate and elongates in the streamwise coordinate as reported in Section 2. Therefore, straighter and thinner channels are obtained in the modified diamond lattice when reducing α. The modified Poiseuille model Eq. (15) already accounts for the effect of the channels thinning through the POCS window $d_{w,T}$. On the other hand, it does not account for the effect of the straighter channels obtained in the modified unit cell. For instance, Fig. 5 shows that straighter streamlines and thus flow path is obtained at same Re_{ds} in the case of the modified diamond lattice

with α = 20°. In this view, the length of the unit cell is given by Eq. (3) and is a function of cos(α). Consequently, the effect of the channel length is captured proportionally to cos(α). In doing so, C' and D' are imposed equal to those of the regular diamond lattice for α = α*$_{Dia}$, and a power-law dependency is proposed:

$$C'(\alpha) = 9.89 \cdot \left(\frac{\cos(\alpha)}{\cos(\alpha_{Dia}^*)} \right)^p \qquad (18)$$

$$D'(\alpha) = 0.25 \cdot \left(\frac{\cos(\alpha)}{\cos(\alpha_{Dia}^*)} \right)^q \qquad (19)$$

where p, q are evaluated through regression of the C' and D' as reported in Fig. 11. Hence, the following final expression is obtained:

$$\frac{\Delta p}{L} = 9.89 \left(\frac{\cos(\alpha)}{\cos(\alpha_{Dia}^*)} \right)^{-2.9} \cdot \frac{\mu u}{\varepsilon d_{w,T}^2} + 0.25 \left(\frac{\cos(\alpha)}{\cos(\alpha_{Dia}^*)} \right)^{-4.5} \cdot \frac{\rho u^2}{\varepsilon^2 d_{w,T}} \qquad (20)$$

which holds for $1 \le Re_{ds} \le 200$, $0.7 \le \varepsilon \le 0.95$, $12.5 \le \alpha \le 54.7°$. Fig. 12 reports a parity plot comparing the model prediction against the CFD data, where a MAPE = 11% is obtained.

5.3. Assessment of anisotropic POCS merit index

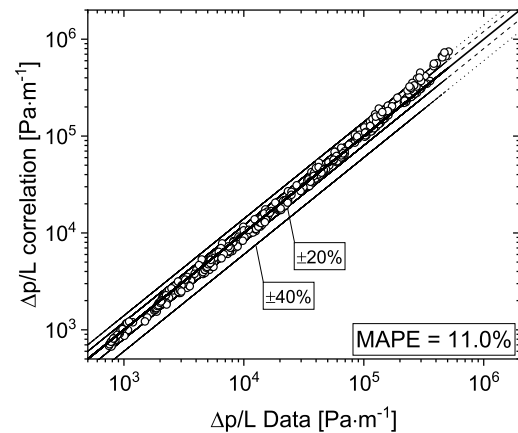The modified diamond lattice performance is hereby compared to

Fig. 12. Parity plot comparing the pressure drop data obtained from CFD simulations and the model prediction for the modified diamond lattice.
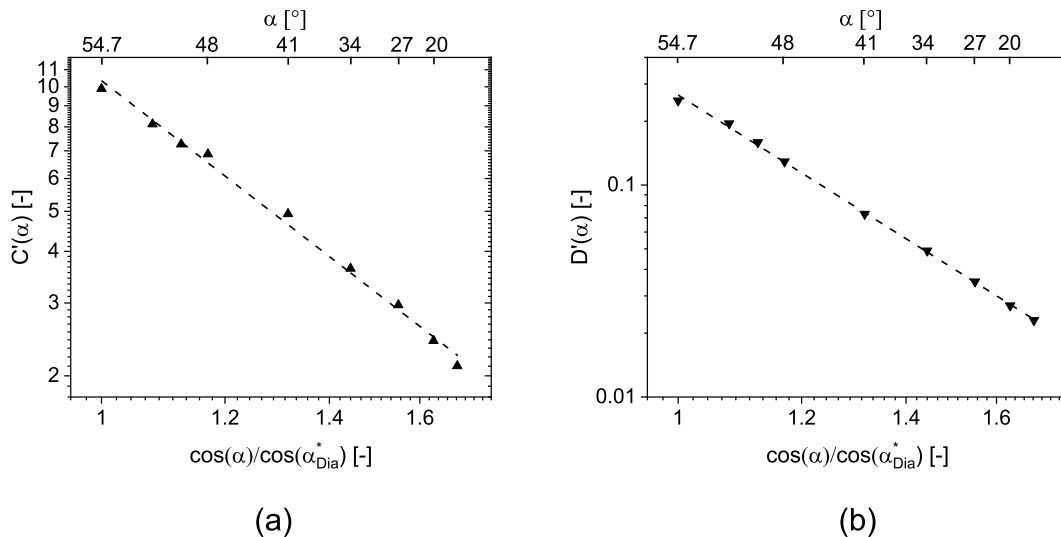

Fig. 11. Regression of the (a) C' coefficient and (b) D' coefficient of the Φ_{ds} as a function of α.

state-of-the-art structured substrates for catalytic applications which are severely affected by a trade-off between the gas-solid mass transfer and the pressure drop, such as in environmental applications. An evaluation of the modified diamond unit cell performance is carried out based on the correlations derived in this work, aiming at determining its behaviour in realistic conditions. Honeycomb monoliths featuring $\varepsilon/OFA = 0.70 – 0.85$ are considered as benchmark for a ceramic and metallic honeycomb, respectively. Conversely, the modified diamond lattice morphological parameters are properly adjusted to provide the best performance.

Fig. 13 compares the overall performance of the modified diamond lattice with that of the honeycomb monolith. In the case of the honeycomb, laminar flow conditions are always obtained in the Re number range of interest ($Re_{dh} < 2300$), thus a constant Sh is obtained in all the flow conditions, whereas the friction factor is inversely dependant on Re [39,42]. Consequently, the M.I. is only a function of the porosity/OFA, and a constant M.I. = 0.27 and 0.40 are obtained for OFA = 0.70 and 0.85, respectively. Conversely, the modified diamond lattice features an increasing Sh with Re, and a linear-quadratic dependency of the pressure drop on the flowrate. This results in a parabolic-like trend of the M.I. in the semi-log plot of Fig. 13. At constant porosity (see Fig. 13(a)), the M.I. increases at increasing α in consistency with the preliminary assessment of the overall performance (see Section 4.1), due to the greater impact of α on the reduction of the friction factor than of Sh. The modified diamond lattice outperforms the honeycomb for $\alpha < 35°$ in a wide range of operative conditions ($5 < Re_{Lchar}\cdot(S_vL_{char})^{-1} < 300$). The maximum of the M.I. is obtained at higher Re_{ds} for decreasing α. This is ascribed to the increase of Re_{ds} where the onset of the vortex shedding occurs (Section 4.2). Indeed, the maximum M.I. is observed for the regular diamond lattice at around $Re_{ds}\cdot(S_vd_s)^{-1} = 20$, whereas for the modified diamond lattice with $\alpha = 20°$ at around $Re_{ds}\cdot(S_vd_s)^{-1} = 50$, namely at slightly lower Re_{ds} of the transition between the regimes. When the transition is reached, the vortex shedding phenomenon causes an increase in the friction factor, which in turns results in a decrease of the M.I.. For the modified diamond lattice at constant $\alpha = 20°$ (see Fig. 13(b)), the M.I. is observed to increase with the porosity in agreement with other cellular substrates' behaviour [13]. Still, a better performance than for the metallic honeycomb can be observed for $\varepsilon > 0.75$.

The analysis of the Merit Index allowed to compare the substrates' overall performance. However, it provides limited quantitative information related to the application of the innovative structured substrates. For instance, standard POCS geometries were proven to be substantially affected by their pressure drop [13]. The reduced friction factor of the hereby proposed geometry represents an enabling factor for such structures in real applications. However, this is achieved with a concomitant reduction of the mass transfer coefficient with respect to the original geometry (see Section 4.1). On top of this, the change of the diamond unit cell morphology as a function of α severely affects the strut diameter (see Fig. 2), which is a crucial aspect for the substrate manufacturing and reproducibility [52]. Therefore, an applied comparison of the performance is carried out in the following Section for realistic substrate designs, aiming at fully defining the optimized POCS behaviour.

6. Performance comparison between structured substrates

Realistic designs of substrates are quantitatively compared in terms of transport coefficient and pressure drop. To do so, CO oxidation diluted in air at 573 K and 1 bar is considered as mass-transfer limited reaction which may realistically occur in an aftertreatment system. Isothermal and steady-state conditions are assumed with a uniform concentration of reactants, thus the performance of the catalytic supports is evaluated using a 1D heterogeneous PFR model (see Section 3.2). In doing so, the performance is evaluated under idealized conditions, neglecting any side effects such as entrance effects, reactants maldistribution and reactor solid wall effects.

A state-of-the-art honeycomb monolith (900 CPSI, 2.5 mils) is considered as benchmark. Modified diamond lattices featuring a porosity of $\varepsilon = 0.9$ are considered to maximize the M.I. with a low pressure drop. Notably, POCS are currently fabricated by additive manufacturing (3D printing). While in aftertreatment systems ceramic supports are mainly employed, 3D printing can be performed for a wide variety of materials (e.g., resins, ceramics, metals) by virtue of the numerous techniques available (e.g., SLA, SLS, SLM) [53–55]. In this view, the modified unit cell POCS is expected not to pose additional problems in manufacturing compared to the conventional shapes, indeed, only the strut diameter is considered as the manufacturing limit being the POCS feature with minimum size. Hence, a minimum strut diameter of $d_s = 200$ μm is assumed to comply with the current manufacturing limit [53–55], however, 3D printing is rapidly progressing and thus details with smaller size may likely become feasible in the forthcoming years.

The geometrical properties of the considered substrates are listed in Table 2. As discussed in Section 2, the modified diamond lattices provide
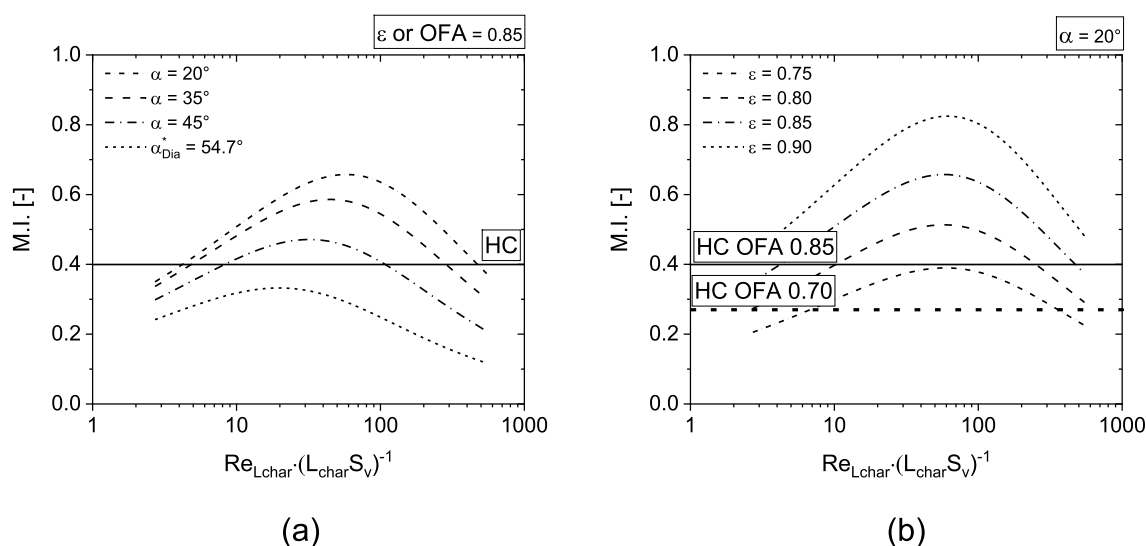

Fig. 13. Merit Index of the modified diamond lattice (a) as a function of α at constant porosity $\varepsilon = 0.85$ and (b) as a function of the porosity at constant $\alpha = 20°$ HC: honeycomb monolith with open frontal area OFA = 0.85 (solid line) and 0.7 (dotted line).

Table 2
Geometrical properties of the compared substrates.

Sample	d_c or $d_{channel}$ [mm]	ε or OFA [-]	S_v [m^{-1}]	L_{char} [mm]
Diamond $\alpha = 20°$	2.592	0.90	1869	0.200
Diamond $\alpha = 35°$	1.649	0.90	1833	0.200
Diamond $\alpha = 45°$	1.436	0.90	1830	0.200
Regular Diamond	1.376	0.90	1843	0.200
Honeycomb 900/2.5	0.847	0.85	4355	0.781

almost constant specific surface area independent of α, whereas the cell size increases by decreasing α.

Fig. 14 shows the mass transfer limited conversion of CO at temperature $T = 573$ K and working fluid velocity (a) $u = 5$ m/s and (b) $u = 15$ m/s. In all conditions, the diamond lattice offers a larger transport coefficient than the honeycomb resulting in up to 20% higher conversion at $u = 5$ m/s and up to 30% higher conversion at 15 m/s. The transport coefficient decreases at decreasing α (e.g., for $u = 15$ m/s, k_v = 1960 and 2850 s^{-1} for $\alpha = 20°$ and $\alpha*_{Dia}$, respectively), resulting in up to 10% difference in conversion between the regular geometry and the modified configuration with $\alpha = 20°$ in full external mass transfer control. On the other hand, the regular diamond lattice shows a 2-fold and 5-fold higher pressure drop than the honeycomb in the two considered conditions (see Table 3). The pressure drop drastically reduces at decreasing α. For instance, in the case of $\alpha = 20°-35°$ even a lower pressure drop than for the honeycomb is achieved at $u = 5$ m/s, and a comparable pressure drop at $u = 15$ m/s.

An additional analysis can be performed by keeping the constraint on the porosity and considering different strut sizes. In particular, Fig. 15(a) shows a contour plot reporting the volumetric mass transfer coefficient k_v (colours) and the pressure drop per unit length $\Delta p/L$ (solid black lines) as a function of d_s and α at porosity $\varepsilon = 0.9$ and velocity $u = 15$ m/s (i.e., at the conditions of Fig. 14(b)). Both the mass transfer coefficient and the pressure drop increase at increasing α, as an effect of the enhanced fluid-solid interaction as reported in Section 4.2, and at decreasing d_s due to the higher specific surface area S_v. Compared to the honeycomb, offering $k_v = 1030$ s^{-1} and 24 kPa·m^{-1}, the regular diamond lattice ensures a better transport coefficient for $d_s < 350$ μm while lower values of d_s are necessary at lower α to overcome the k_v of the honeycomb (e.g., $d_s < 300$ μm for $\alpha = 20°$). An $\alpha < 50°$ is necessary to obtain a lower pressure drop than for the honeycomb, however, an even lower α is required to achieve a lower pressure drop with a concomitant higher k_v. In this view, a Pareto plot (Fig. 15(b)) is extracted from all the

conditions of Fig. 15(a) to provide the highest possible transfer coefficient k_v at a given value of pressure drop. The honeycomb (HC) $\Delta p/L$ and k_v are reported for reference as solid black lines. Accordingly, four quadrants are obtained from the reference lines. (i) On the bottom left, structures providing lower pressure drop and transport coefficient than the honeycomb are obtained. (ii) On the bottom right, structures providing poorer transport coefficient and higher pressure drop are found. (iii) On the top right, structures having better transport coefficient at the expense of a higher pressure drop are obtained. (iv) Finally, on the top left better transport coefficient and lower pressure drop are obtained, representing the most desirable condition. Hence, the Pareto plot (full symbols) reports the highest possible k_v against the pressure drop, and such a condition is achieved for α around 17° for all the strut diameters considered, while the strut diameter (empty red symbols) is tuned by manipulating the unit cell size. The Pareto plot intersects the HC reference lines in the quadrants i, iii, iv, accordingly, different performances can be obtained. In particular, the modified diamond lattice may provide up to a 2-fold increase in the mass transfer coefficient at the same pressure drop as for the honeycomb, or a reduction in the pressure drop with the same mass transfer performance, in agreement with the Merit Index (Fig. 13). Notably, from a manufacturing perspective a feasible range of $200 < d_s < 500$ μm is obtained for $\Delta p/L < 20$ kPa·m^{-1}. Instead, to obtain higher $\Delta p/L$ (i.e., higher k_v) up to a $d_s = 150$ μm is required. Thus, the constraint of $d_s > 200$ μm would require a lower angle of attack α, higher cell size d_c or lower porosity ε. Even so, it should be kept in mind that additive manufacturing rapidly developed and advanced throughout the last decade, and further improvement is expected in the next years, which may lead to a higher resolution in the production of objects' minimum features.

In conclusion, the analyses of Figs. 14 and 15 were carried out under idealized conditions (i.e., steady-state isothermal system with uniform concentration of CO), where the best performance of the honeycomb is usually obtained. Hence, the analyses reveal the high potential of the

Table 3
Pressure drop of the compared substrates at the conditions of Fig. 14.

Sample	$\Delta p/L$ at $u = 5$ m/s [Pa·m^{-1}]	$\Delta p/L$ at $u = 15$ m/s [Pa·m^{-1}]
Diamond $\alpha = 20°$	4800	23500
Diamond $\alpha = 35°$	6500	35000
Diamond $\alpha = 45°$	9400	55000
Regular Diamond	16200	106000
Honeycomb 900/2.5	7800	23500

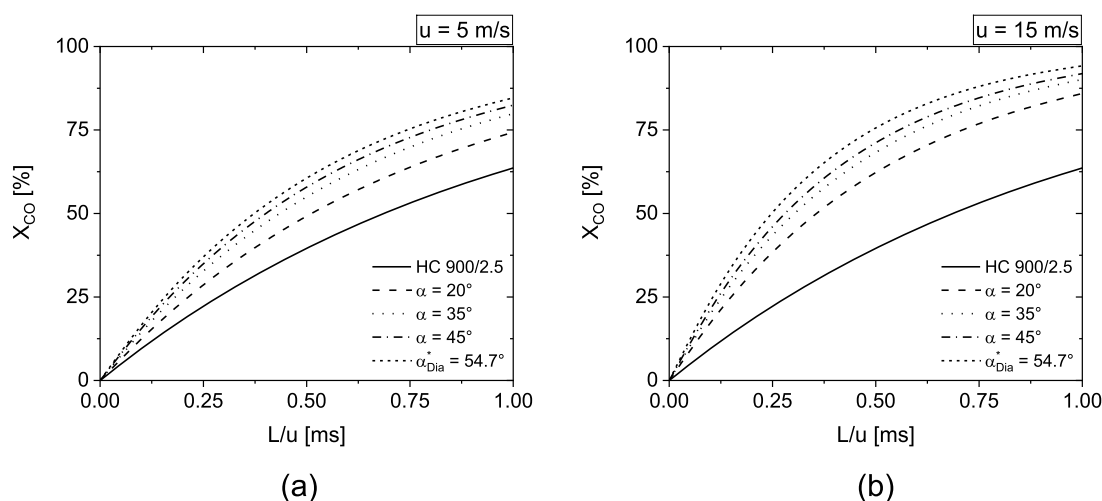**Fig. 14.** Mass transfer limited CO conversion of the standard honeycomb monolith 900/2.5 and of the modified diamond lattice at changing α and constant porosity $\varepsilon = 0.9$ and $d_s = 200$ μm. CO oxidation in air at $T = 573$ K, (a) $u = 5$ m/s and (b) $u = 15$ m/s.
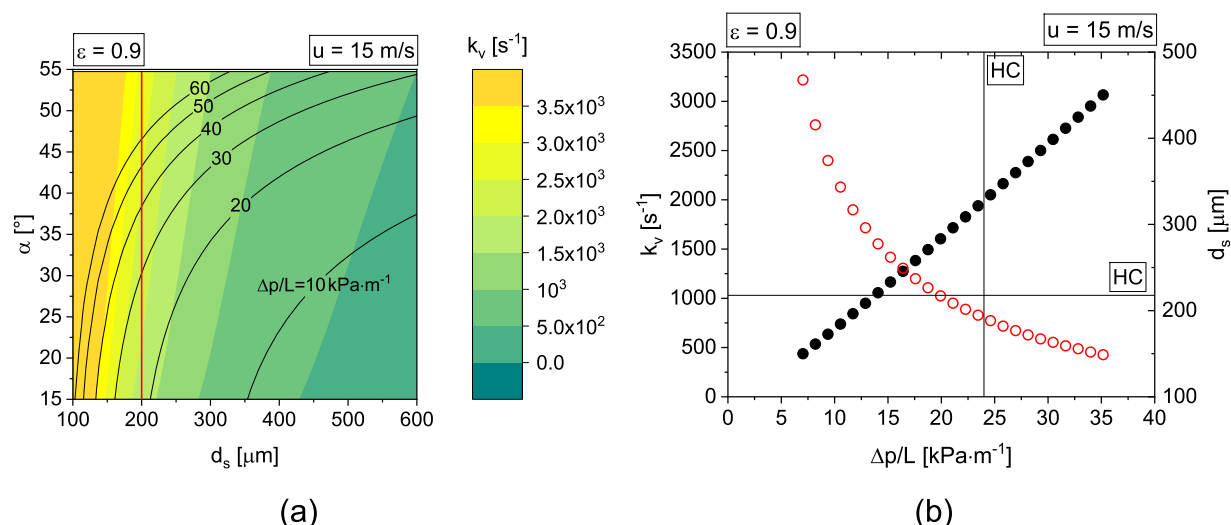
Fig. 15. (a) Contour plot of the mass transfer coefficient k_v (colours) and the pressure drop (solid black lines) as a function of d_s and α at $\varepsilon = 0.9$ and $u = 15$ m/s. Solid red line: d_s limit of manufacturing. (b) Pareto plot of k_v against the pressure drop (full symbols) and corresponding d_s (empty symbols).

modified diamond unit cell POCS for process intensification. Other aspects such as flow and reactant concentration distribution inside the reactor will be considered in follow-up works. In this view, the open-cell structure of the POCS may offer further improvements.

7. Summary and conclusions

In this work, we propose a novel approach for the intensification of mass-transfer limited catalytic reactors by optimization of the trade-off between interphase gas-solid mass transfer and pressure drop in Periodic Open Cellular Structures, based on non-isotropic unit cells. This work reveals that the manipulation of the cell shape leading to non-isotropic geometries offers high potential for intensification.

The diamond lattice, which was proven in earlier works to offer the best trade-off between gas-solid mass transfer and pressure drop, was manipulated to modify the fluid-solid interaction in view of further boosting such a trade-off. In doing so, the angle between the struts and the fluid flow direction was modified, obtaining an advanced geometry with anisotropic permeability along the streamwise and transverse coordinates. As a preliminary analysis, the overall performance of the POCS were directly evaluated through CFD simulations in terms of the Merit Index. A two-fold increase of this trade-off index could be achieved, highlighting the benefit of the advanced POCS design. According to such analysis, the improvement of the trade-off was observed by decreasing the angle between the struts and the flow direction, thus obtaining a stretched unit cell along the streamwise direction and shrunken in the transverse directions. The fundamental investigation was thus carried out for such configurations. In particular, the effects of the working fluid flowrate, the angle of attack α of the struts and the POCS porosity and cell size on the transport properties (Sherwood number, Sh_{ds}) and friction factor Φ_{ds} were examined. The angle α was found to mostly influence the fluid dynamics inside the lattice. Depending on the fluid flowrate, two flow regimes were observed, namely, a laminar regime and an unsteady laminar regime. By reducing α, the threshold for the transition between the two regimes was observed to increase from a Reynolds number around 32 in the case of the regular geometry up to 64 at the lowest α. An interdependency of Sh_{ds} and Φ_{ds} on α and the Reynolds number was found. In agreement with previous work on the standard POCS shape, the effect of the cell size on Sh_{ds} and Φ_{ds} was found to be implicitly accounted for by their dependency on the Reynolds number, while they decreased at the increasing support porosity. In particular, an average dependency of Sh_{ds} on the porosity $\varepsilon^{-1.5}$ was identified in agreement with previous findings for the regular

lattice.

After fundamental investigations, simplified models were proposed to predict the dimensionless transport coefficient and friction factor as a function of the flow conditions, substrate porosity and strut tilting angle. The derived correlations were employed to compare the modified diamond lattice performance with the state-of-the-art structured substrate, i.e., the honeycomb monolith. Significantly better overall performance is provided by the modified diamond lattice. Up to a two-fold higher mass transfer coefficient compared to the honeycomb was observed at same pressure drop. In conclusion, the analysis highlights the high potential in the application of modified POCS as enhanced structured substrates for process intensification.

Declaration of Competing Interest

The authors declare that they have no known competing financial interests or personal relationships that could have appeared to influence the work reported in this paper.

Data availability

Data will be made available on request.

Acknowledgments

Supplementary materials

Supplementary material associated with this article can be found, in the online version, at doi:10.1016/j.cep.2023.109613.

References

[1] A. Inayat, J. Schwerdtfeger, H. Freund, C. Körner, R.F. Singer, W. Schwieger, Periodic open-cell foams: pressure drop measurements and modeling of an ideal tetrakaidecahedra packing, Chem. Eng. Sci. 66 (2011) 2758–2763, https://doi.org/10.1016/j.ces.2011.03.031.

[2] M. Ambrosetti, G. Groppi, W. Schwieger, E. Tronconi, H. Freund, Packed periodic open cellular structures – an option for the intensification of non-adiabatic

catalytic processes, Chem. Eng. Process. - Process Intensif. 155 (2020), 108057, https://doi.org/10.1016/j.cep.2020.108057.

[3] M. Bracconi, M. Ambrosetti, M. Maestri, G. Groppi, E. Tronconi, Chemical engineering and processing - process intensification analysis of the effective thermal conductivity of isotropic and anisotropic periodic open cellular structures for the intensification of catalytic processes, Chem. Eng. Process. - Process Intensif. 158 (2020), 108169, https://doi.org/10.1016/j.cep.2020.108169.

[4] K. Dubil, T. Wetzel, B. Dietrich, Modelling steady-state convective heat transfer in different periodic open cellular structures (POCS) – A superposition approach, Int. J. Heat Mass Transf. 200 (2023), 123546, https://doi.org/10.1016/j.ijheatmasstransfer.2022.123546.

[5] L. Fratalocchi, G. Groppi, C.G. Visconti, L. Lietti, E. Tronconi, Adoption of 3D printed highly conductive periodic open cellular structures as an effective solution to enhance the heat transfer performances of compact Fischer-Tropsch fixed-bed reactors, Chem. Eng. J. 386 (2020), 123988, https://doi.org/10.1016/j.cej.2019.123988.

[6] L. Fratalocchi, G. Groppi, C.G. Visconti, L. Lietti, E. Tronconi, Packed-POCS with skin: a novel concept for the intensification of non-adiabatic catalytic processes demonstrated in the case of the Fischer-Tropsch synthesis, Catal. Today. 383 (2022) 15–20, https://doi.org/10.1016/j.cattod.2020.12.031.

[7] F.S. Franchi, M. Ambrosetti, R. Balzarotti, M. Bracconi, G. Groppi, E. Tronconi, Rich H2 catalytic oxidation as a novel methodology for the evaluation of mass transport properties of 3D printed catalyst supports, Catal. Today 383 (2022) 123–132, https://doi.org/10.1016/j.cattod.2021.04.004.

[8] G. Do, M. Geißelbrecht, W. Schwieger, H. Freund, Additive manufacturing of interpenetrating periodic open cellular structures (interPOCS) with in operando adjustable flow characteristics, Chem. Eng. Process. - Process Intensif. 148 (2020), 107786, https://doi.org/10.1016/j.cep.2019.107786.

[9] M. Klumpp, A. Inayat, J. Schwerdtfeger, C. Körner, R.F. Singer, H. Freund, W. Schwieger, Periodic open cellular structures with ideal cubic cell geometry: effect of porosity and cell orientation on pressure drop behavior, Chem. Eng. J. 242 (2014) 364–378, https://doi.org/10.1016/j.cej.2013.12.060.

[10] M. Lämmermann, G. Horak, W. Schwieger, H. Freund, Periodic open cellular structures (POCS) for intensification of multiphase reactors: liquid holdup and two-phase pressure drop, Chem. Eng. Process. - Process Intensif. 126 (2018) 178–189, https://doi.org/10.1016/j.cep.2018.02.027.

[11] C. Busse, H. Freund, W. Schwieger, Intensification of heat transfer in catalytic reactors by additively manufactured periodic open cellular structures (POCS), Chem. Eng. Process. Process Intensif. 124 (2018) 199–214, https://doi.org/10.1016/j.cep.2018.01.023.

[12] M. Lämmermann, W. Schwieger, H. Freund, Experimental investigation of gas-liquid distribution in periodic open cellular structures as potential catalyst supports, Catal. Today. 273 (2016) 161–171, https://doi.org/10.1016/j.cattod.2016.02.049.

[13] C. Ferroni, F.S. Franchi, M. Ambrosetti, M. Bracconi, G. Groppi, M. Maestri, E. Tronconi, Numerical and experimental investigation of pressure drop in periodic open cellular structures for intensification of catalytic processes, ACS Eng. Au. 2 (2022) 118–133, https://doi.org/10.1021/acsengineeringau.1c00034.

[14] C. Ferroni, M. Bracconi, M. Ambrosetti, M. Maestri, G. Groppi, E. Tronconi, A fundamental investigation of gas/solid heat and mass transfer in structured catalysts based on Periodic Open Cellular Structures (POCS), Ind. Eng. Chem. Res. 60 (2021) 10522–10538, https://doi.org/10.1021/acs.iecr.1c00215.

[15] G. Littwin, S. Röder, H. Freund, Systematic experimental investigations and modeling of the heat transfer in additively manufactured periodic open cellular structures with diamond unit cell, Ind. Eng. Chem. Res. 60 (2021) 6753–6766, https://doi.org/10.1021/acs.iecr.0c06210.

[16] E. Bianchi, W. Schwieger, H. Freund, Assessment of periodic open cellular structures for enhanced heat conduction in catalytic fixed-bed reactors, Adv. Eng. Mater. 18 (2016) 608–614, https://doi.org/10.1002/adem.201500356.

[17] V. Papetti, P. Dimopoulos Eggenschwiler, A. Della Torre, F. Lucci, A. Ortona, G. Montenegro, Additive Manufactured open cell polyhedral structures as substrates for automotive catalysts, Int. J. Heat Mass Transf. 126 (2018) 1035–1047, https://doi.org/10.1016/j.ijheatmasstransfer.2018.06.061.

[18] O. Santoliquido, G. Bianchi, P. Dimopoulos Eggenschwiler, A. Ortona, Additive manufacturing of periodic ceramic substrates for automotive catalyst supports, Int. J. Appl. Ceram. Technol. 14 (2017) 1164–1173, https://doi.org/10.1111/ijac.12745.

[19] O. Santoliquido, F. Camerota, M. Pelanconi, D. Ferri, M. Elsener, P. D. Eggenschwiler, A. Ortona, Structured alumina substrates for environmental catalysis produced by stereolithography, Appl. Sci. (2021) 11, https://doi.org/10.3390/app11178239.

[20] A. Chaudhari, P. Ekade, S. Krishnan, Experimental investigation of heat transfer and fluid flow in octet-truss lattice geometry, Int. J. Therm. Sci. 143 (2019) 64–75, https://doi.org/10.1016/j.ijthermalsci.2019.05.003.

[21] P. Ekade, S. Krishnan, Fluid flow and heat transfer characteristics of octet truss lattice geometry, Int. J. Therm. Sci. 137 (2019) 253–261, https://doi.org/10.1016/j.ijthermalsci.2018.11.031.

[22] J.Y. Ho, K.C. Leong, T.N. Wong, Experimental and numerical investigation of forced convection heat transfer in porous lattice structures produced by selective laser melting, Int. J. Therm. Sci. 137 (2019) 276–287, https://doi.org/10.1016/j.ijthermalsci.2018.11.022.

[23] I. Kaur, P. Singh, Endwall heat transfer characteristics of octahedron family lattice-frame materials, Int. Commun. Heat Mass Transf. 127 (2021), 105522, https://doi.org/10.1016/j.icheatmasstransfer.2021.105522.

[24] F. Lucci, A. Della Torre, G. Montenegro, R. Kaufmann, P. Dimopoulos Eggenschwiler, Comparison of geometrical, momentum and mass

transfer characteristics of real foams to Kelvin cell lattices for catalyst applications, Int. J. Heat Mass Transf. 108 (2017) 341–350, https://doi.org/10.1016/j.ijheatmasstransfer.2016.11.073.

[25] M. Sun, M. Li, C. Hu, L. Yang, Y. Song, D. Tang, J. Zhao, Comparison of forced convective heat transfer between pillar and real foam structure under high Reynolds number, Appl. Therm. Eng. 182 (2020), 116130, https://doi.org/10.1016/j.applthermaleng.2020.116130.

[26] A. Della Torre, F. Lucci, G. Montenegro, A. Onorati, P. Dimopoulos Eggenschwiler, E. Tronconi, G. Groppi, CFD modeling of catalytic reactions in open-cell foam substrates, Comput. Chem. Eng. 92 (2016) 55–63, https://doi.org/10.1016/j.compchemeng.2016.04.031.

[27] V. Chandra, S. Das, E.A.J.F. Peters, J.A.M. Kuipers, Direct numerical simulation of hydrodynamic dispersion in open-cell solid foams, Chem. Eng. J. 358 (2019) 1305–1323, https://doi.org/10.1016/j.cej.2018.10.017.

[28] L. Giani, G. Groppi, E. Tronconi, Mass-transfer characterization of metallic foams as supports for structured catalysts, Ind. Eng. Chem. Res. 44 (2005) 4993–5002, https://doi.org/10.1021/ie0490886.

[29] D. Micale, C. Ferroni, R. Uglietti, M. Bracconi, M. Maestri, Computational fluid dynamics of reacting flows at surfaces: methodologies and applications, Chemie-Ingenieur-Technik 94 (2022) 634–651, https://doi.org/10.1002/cite.202100196.

[30] M. Maestri, A. Cuoci, Coupling CFD with detailed microkinetic modeling in heterogeneous catalysis, Chem. Eng. Sci. 96 (2013) 106–117, https://doi.org/10.1016/j.ces.2013.03.048.

[31] B.M. Adams, W.J. Bohnhoff, K.R. Dalbey, M.S. Ebeida, J.P. Eddy, M.S. Eldred, R.W. Hooper, P.D. Hough, K.T. Hu, J.D. Jakeman, M. Khalil, K.A. Maupin, J.A. Monschke, E.M. Ridgway, A.A. Rushdi, D. Thomas, J.A. Stephens, L.P. Swiler, J.G. Winokur, Dakota User's Manual v 6.15, (2021).

[32] M. Bracconi, M. Ambrosetti, O. Okafor, V. Sans, X. Zhang, X. Ou, C.P. Da Fonte, X. Fan, M. Maestri, G. Groppi, E. Tronconi, Investigation of pressure drop in 3D replicated open-cell foams: coupling CFD with experimental data on additively manufactured foams, Chem. Eng. J. 377 (2019), 120123, https://doi.org/10.1016/j.cej.2018.10.060.

[33] M. Bracconi, M. Ambrosetti, M. Maestri, G. Groppi, E. Tronconi, A fundamental investigation of gas/solid mass transfer in open-cell foams using a combined experimental and CFD approach, Chem. Eng. J. 352 (2018) 558–571, https://doi.org/10.1016/j.cej.2018.07.023.

[34] A. Cuoci, A. Frassoldati, T. Faravelli, E. Ranzi, OpenSMOKE++: an object-oriented framework for the numerical modeling of reactive systems with detailed kinetic mechanisms, Comput. Phys. Commun. 192 (2015) 237–264, https://doi.org/10.1016/j.cpc.2015.02.014.

[35] S. Gordon, B.J. McBride, Computer Program for Calculation of Complex Chemical Equilibrium Compositions and Applications I. Analysis, NASA Ref. Publ. 1311. (1994) 58. doi:NASA RP-1311.

[36] J.O. Hirschfelder, C.F. Curtiss, R.B. Bird, Molecular theory of gases and liquids, Phys. Today 8 (1955) 17, https://doi.org/10.1063/1.3061949. –17.

[37] C.F. Curtiss, J.O. Hirschfelder, Transport properties of multicomponent gas mixtures, J. Chem. Phys. 17 (1949) 550–555, https://doi.org/10.1063/1.1747319.

[38] H. Jasak, A. Jemcov, Z. Tukovic, OpenFOAM : a C ++ library for complex physics simulations, Int. Work. Coupled Methods Numer. Dyn. m (2007) 1–20. https://foam-extend.fsb.hr/wp-content/uploads/2018/04/Jasak_Jemcov_Tukovic_OpenFOAM_C_library_for_complex_physics_simulations_2007.pdf (accessed September 10, 2019).

[39] E. Tronconi, P. Forzatti, Adequacy of lumped parameter models for SCR reactors with monolith structure, AIChE J. 38 (1992) 201–210, https://doi.org/10.1002/aic.690380205.

[40] S. Rebughini, A. Cuoci, M. Maestri, Hierarchical analysis of the gas-to-particle heat and mass transfer in micro packed bed reactors, Chem. Eng. J. 289 (2016) 471–478, https://doi.org/10.1016/j.cej.2015.12.089.

[41] G. Groppi, A. Belloli, E. Tronconi, P. Forzatti, A comparison of lumped and distributed models of monolith catalytic combustors, Chem. Eng. Sci. 50 (1995) 2705–2715, https://doi.org/10.1016/0009-2509(95)00099-Q.

[42] R.K. Shah, A.L. London, Discussion—An Overview for the Designer and the Applied Mathematician, Academic Press, 1978, https://doi.org/10.1016/b978-0-12-020051-1.50022-x.

[43] K. Ishimi, S. Koroyasu, H. Hikita, Mass transfer in creeping flow past periodic arrays of cylinders, J. Chem. Eng. JAPAN. 20 (1987) 492–498, https://doi.org/10.1252/jcej.20.492.

[44] H. Fugmann, L. Schnabel, B. Frohnapfel, Heat transfer and pressure drop correlations for laminar flow in an in-line and staggered array of circular cylinders, Numer. Heat Transf. Part A Appl. 75 (2019) 1–20, https://doi.org/10.1080/10407782.2018.1562741.

[45] R. Hilpert, Wärmeabgabe von geheizten Drähten und Rohren im Luftstrom, Forsch. Auf Dem Gebiete Des Ingenieurwesens 4 (1933) 215–224, https://doi.org/10.1007/BF02719754.

[46] VDI-Gesellschaft Verfahrenstechnik und Chemieingenieurwesen., VDI Heat Atlas, Springer, 2010. doi:10.1007/978-3-540-77877-6.

[47] L. Zhao, S.M. Ryan, J.K. Ortega, S. Ha, K.W. Sharp, J.K. Guest, K.J. Hemker, T. P. Weihs, Experimental investigation of 3D woven Cu lattices for heat exchanger applications, Int. J. Heat Mass Transf. 96 (2016) 296–311, https://doi.org/10.1016/j.ijheatmasstransfer.2015.12.059.

[48] F.E. Teruel, Rizwan-Uddin, Characterization of a porous medium employing numerical tools: permeability and pressure-drop from Darcy to turbulence, Int. J. Heat Mass Transf. 52 (2009) 5878–5888, https://doi.org/10.1016/j.ijheatmasstransfer.2009.07.017.

[49] M.H.J. Pedras, M.J.S. De Lemos, Macroscopic turbulence modeling for incompressible flow through undeformable porous media, Int. J. Heat Mass Transf. 44 (2001) 1081–1093, https://doi.org/10.1016/S0017-9310(00)00202-7.

[50] E. Reichelt, M. Jahn, Generalized correlations for mass transfer and pressure drop in fiber-based catalyst supports, Chem. Eng. J. 325 (2017) 655–664, https://doi.org/10.1016/j.cej.2017.05.119.

[51] D. Nemec, J. Levec, Flow through packed bed reactors: 1. Single-phase flow, Chem. Eng. Sci. 60 (2005) 6947–6957, https://doi.org/10.1016/j.ces.2005.05.068.

[52] M. Bracconi, Chemical Engineering and Processing - Process Intensification Intensification of catalytic reactors : a synergic effort of Multiscale Modeling, Machine Learning and Additive Manufacturing, Chem. Eng. Process. - Process Intensif. 181 (2022), 109148, https://doi.org/10.1016/j.cep.2022.109148.

[53] Z. Chen, Z. Li, J. Li, C. Liu, C. Lao, Y. Fu, C. Liu, Y. Li, P. Wang, Y. He, 3D printing of ceramics: a review, J. Eur. Ceram. Soc. 39 (2019) 661–687, https://doi.org/10.1016/j.jeurceramsoc.2018.11.013.

[54] X. Wang, M. Jiang, Z. Zhou, J. Gou, D. Hui, 3D printing of polymer matrix composites: a review and prospective, Compos. Part B Eng. 110 (2017) 442–458, https://doi.org/10.1016/j.compositesb.2016.11.034.

[55] T.D. Ngo, A. Kashani, G. Imbalzano, K.T.Q. Nguyen, D. Hui, Additive manufacturing (3D printing): a review of materials, methods, applications and challenges, Compos. Part B Eng. 143 (2018) 172–196, https://doi.org/10.1016/j.compositesb.2018.02.012.